Adsorption of aspartic acid on Ni{100}: a combined experimental and theoretical study

LANGMUIR

pubs.acs.org/Langmuir Article

Adsorption of Aspartic Acid on Ni{100}: A Combined Experimental and Theoretical Study

Wilson Quevedo, Jorge Ontaneda, Alexander Large, Jake M. Seymour, Roger A. Bennett, Ricardo Grau-Crespo,* and Georg Held*

Cite This: https://dx.doi.org/10.1021/acs.langmuir.0c01175 Read Online

ACCESS | Metrics & More | Article Recommendations | Supporting Information

ABSTRACT: Understanding the interaction of amino acids with metal surfaces is essential for the rational design of chiral modifiers able to confer enantioselectivity to metal catalysts. Here, we present an investigation of the adsorption of aspartic acid (Asp) on the Ni{100} surface, using a combination of synchrotron X-ray photoelectron spectroscopy (XPS), near-edge X-ray absorption fine structure, and density functional theory simulations. Based on the combined analysis of the experimental and simulated data, we can identify the dominant mode of adsorption as a pentadentate configuration with three O atoms at the bridge sites of the surfaces, and the remaining oxygen atom and the amino nitrogen are located on atop sites. From temperature-programmed XPS measurements, it was found that Asp starts decomposing above 400 K, which is significantly higher than typical decomposition temperatures of smaller organic molecules on Ni surfaces. Our results offer valuable insights into understanding the role of Asp as a chiral modifier of nickel catalyst surfaces in enantioselective hydrogenation reactions.

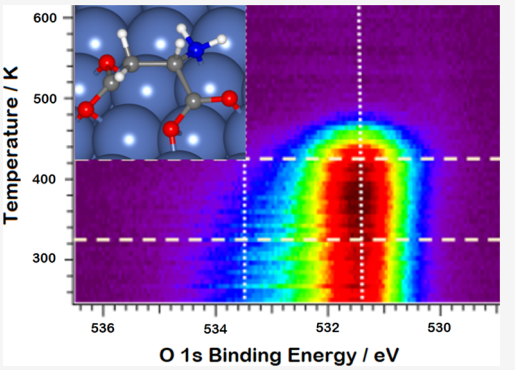

INTRODUCTION

Over the last decades, there has been a growing demand for optically pure drugs and compounds.[1] Because heterogeneous catalysis is more environmentally friendly than homogeneous catalysis, the development of heterogeneous catalysts for the synthesis of enantiopure chemical products offers great benefits.[2−5] Heterogeneous chiral catalysts can be prepared by modifying nonchiral surfaces using the so-called chiral modifiers. The modifier molecules act as precursors that interact with and modify the catalyst metal surface, conferring a chiral behavior that enhances the production of one enantiomer over the other during the catalytic reaction.

One of the best-studied examples in this context is the chiral modification of Ni catalysts with tartaric acid (TA) or amino acids to enable enantioselective hydrogenation of β-ketoesters, such as methyl acetoacetate (MAA).[2−4,6,7] This reaction system is well characterized in terms of macroscopic parameters, for example, temperature, pH, reaction yields, and enantiomeric excess, but still poorly understood in terms of molecular level interactions. In general, one finds higher enantiomeric excess at typical reaction temperatures (25−100 °C) for dicarboxylic modifiers, such as TA, glutamic acid (Glu), or aspartic acid (Asp), compared to simple amino acid, such as alanine (Ala). It has been hypothesized that chiral modification incorporates physical effects, such as substrate reconstruction and/or supramolecular assemblies of the modifier with solvents.[4,7−9] The latter idea is supported by studies that show that both the reaction rate and optical yield are significantly affected by the polarity of the solvent and the pH used in the modification.

In recent years, a significant body of research has been devoted to studying the molecular level interactions of these organic compounds with Ni{111}, {100}, and {110} single-crystal surfaces, employing surface science techniques such as temperature-programmed (TP) desorption, infrared spectroscopy, scanning tunneling microscopy (STM), X-ray photoelectron spectroscopy (XPS), and near-edge X-ray absorption fine structure (NEXAFS) spectroscopy. These include studies of just the modifiers (TA, Glu, and Ala)[10−16] or reactants (MAA)[17,18] and coadsorption studies of reactants and modifiers (MAA with TA, Glu, and Asp) in vacuum and under (wet) reaction conditions.[8,9,19−21] The latter research, carried out by Baddeley's group, found strong evidence for a one-to-one interaction between the chiral modifier and MAA. Recent work from our group[17,18] has shown that MAA adsorbs on Ni{100} and Ni{111} as deprotonated enolate species, with bidentate coordination through the C−O groups. The

Received: April 22, 2020
Revised: July 17, 2020
Published: July 24, 2020

molecular plane is tilted with respect to the surface plane, between 49 and 63°, thus breaking the local symmetry of the adsorption complex. The role of a chiral modifier could simply be to ensure that the tilt is always in the same direction so that the reaction with surface hydrogen occurs from the same side for all MAA molecules; this would be enough to lead to enantiopure products.

Our recent work on alanine on Ni{111},[15,16] together with numerous studies of amino acids on copper and palladium single-crystal surfaces,[22−39] has indicated that amino acid modifiers preferably adsorb as anions, forming surface bonds through the two carboxylate oxygen atoms and the nitrogen atom of the amino group. In addition, there is a strong tendency to form hydrogen bonds with other molecules on the surface, which, in some cases, leads to the loss of surface coordination and/or the formation of zwitterionic species. This has been observed for Ala on Pd{111} and Ni{111} for higher coverages.[15,16,24,32]

In the present study, we concentrate on the surface chemistry and adsorption geometry of Asp on Ni{100}. There are very few studies of model catalyst systems involving Ni{100} despite the fact that this surface termination is the second most abundant of Ni nanoparticles, after {111}. Asp ($HOOCCH(NH_2)CH_2COOH$) is one of the most abundant amino acids in nature and similar in size to TA (HOOCCH-(OH)C H(OH)COOH). It has three functional groups: α-amino group (α-NH_2), α-carboxyl group (α-COOH), and β-carboxyl group (β-COOH) which can interact with the metal surface. By using a combination of XPS, TP-XPS, and NEXAFS under ultrahigh vacuum (UHV) conditions and computer simulations, we determine the adsorption geometry and thermal stability of the Asp modifier on Ni{100}. This will provide further insight into how chiral modifiers can stereodirect the hydrogenation of β-ketoesters on Ni surfaces.

METHODOLOGY

Experimental Methods. The XPS and NEXAFS experiments were performed in the Elettra synchrotron in Trieste (Italy) at the UHV end station of the SUPERESCA undulator beamline, which provides a horizontally polarized X-ray beam. The base pressures in the preparation and analysis chambers were in the 10^{-10} and 10^{-11} mbar range, respectively. The Ni single crystal (supplier MaTecK; diameter 10 mm; thickness 1.5 mm) with {100} surface orientation was mounted via spot-welded Ta wires onto the base of a liquid nitrogen-cooled cold finger. It could be heated indirectly by a filament mounted close to the back face of the sample. The sample temperature was measured through a spot-welded thermocouple and controlled using a programmable temperature controller. Sample cleaning was achieved by several cycles of short (10 min) Ar^+ sputtering at room temperature with subsequent annealing to 670 K to desorb volatile adsorbates, such as CO. It was found that higher annealing temperatures lead to significant segregation of carbon from the bulk, which could not be completely avoided even at 670 K. The level of sample cleanliness was confirmed by XPS. L-(+)-Asp was dosed from a home-built evaporator, which consisted of a stainless-steel crucible containing a glass capillary filled with Asp powder. The evaporator was mounted in the line of sight of the sample at a distance of ca. 25 cm. Deposition was performed by resistively heating the crucible to 184−186 °C (measured through a thermocouple spot-welded to the crucible).[40] A gate valve between the sample and evaporator allowed accurate control of dosing times. When the gate valve was open, a pressure increase from 10^{-10} mbar to the low 10^{-9} mbar range was observed in the preparation chamber. Because of differences in pumping speed (most likely due to fluctuations in the cold finger temperature), there was no good correlation between measured pressure/dosing time and surface coverage; hence, the coverage was determined by XPS. Typically, deposition times of 30−45 min were needed to deposit a saturated chemisorbed Asp layer for the clean substrate Ni{100} (see below).

XPS and NEXAFS spectra were recorded using a Specs Phoibos 150 Electron energy analyzer. C 1s, N 1s, and O 1s spectra were recorded with photon energies of 400, 510, and 650 eV, respectively, and pass energies of 5 eV (C 1s) and 10 eV (N 1s and O 1s), which resulted in an overall energy resolution of 0.22−0.31 eV. All spectra, shown here, are normalized with respect to the low binding energy (BE) background. TP-XPS data were recorded by heating the sample at a constant rate of 5 K min^{-1} in front of the analyzer, while continuously measuring sequences of fast C 1s, N 1s, and O 1s spectra. The data acquisition time for one sequence of spectra was approximately 70 s, that is, the temperature difference between two consecutive spectra of the same type was about 5.8 K.

NEXAFS spectra were acquired in the O K-edge region by recording the O KLL Auger signal at a kinetic energy of 507 ± 5 eV. Three angles of incidence were used for determining the orientation of Asp with respect to the surface: θ = 0° (normal incidence), 35, and 70°, where θ refers to the angle between the incoming X-ray beam and the surface normal. Photon energy calibration was confirmed by measuring the oxygen K-edge π^*-resonance of CO on Ni{100}, which is within the error limit of literature data[41,42] (534.0 eV vs 533.7 eV in this work). The spectra were divided by the drain current of the last refocusing mirror in order to correct for the transmission of the beamline. Substrate features were removed by subtracting spectra of the clean surface from spectra of the adsorbate-covered surface, measured and treated in the same way. Finally, in order to allow a comparison between spectra measured at different angles, all spectra were normalized at 565 eV, which is above all oxygen absorption resonances.

Computational Methods. For the purpose of density functional theory (DFT) modeling, the Ni{100} surface was represented by a periodic slab of four atomic layers, as reported in previous theoretical investigations of molecular adsorption on this surface,[18,43,44] giving well-converged results for both adsorption energies and geometries.[45] Only the two uppermost Ni layers were relaxed; the two bottom layers were fixed in their bulk positions. This procedure accelerates the convergence of calculated surface properties with respect to the thickness of the simulation slab.[46,47] A vacuum gap of 12 Å separates each slab from its periodic images. Laterally, the supercell consisted of (5 × 5) surface unit cells; therefore, the adsorption of one molecule for every 25 surface Ni atoms gives a surface coverage of 0.04 ML. For the simulation of the isolated (gas-phase) Asp molecule, a large periodic cage was employed, ensuring that each molecule was separated from its images by at least 12 Å.

DFT calculations were performed using plane-wave expansions of the wave functions, as implemented in the VASP code.[48,49] We used a functional based on the generalized gradient approximation (GGA) in the form of the revised Perdew−Burke−Ernzerhof (revPBE) exchange−correlation

https://dx.doi.org/10.1021/acs.langmuir.0c01175
Langmuir XXXX, XXX, XXX−XXX

functional.[50] To account for van der Waals interactions, we used the DFT-D3 method with Becke−Johnson damping.[51,52] This combination of functional and dispersion correction has been shown to be the most robust among GGA functionals in the description of main group thermochemistry, reaction kinetics, and noncovalent interactions[53,54] and has been used successfully in our previous studies of MAA adsorption on Ni surfaces.[17,18] However, we have checked that using the standard GGA functional by PBE[55] with the same dispersion correction leads to, essentially, the same results in terms of relative adsorption energies for different configurations (the absolute adsorption energies with PBE-D3 were ∼0.1 eV less negative than those with revPBE-D3). As nickel is a ferromagnetic metal, all calculations included spin polarization. The effect of core electrons on the valence electron density was described with the projected augmented wave (PAW) method.[56,57] The core electrons (1s in C, O, and N and up to 3p in Ni) were kept frozen at their atomic reference states. The number of plane waves in the slab calculations was limited by a kinetic energy cutoff of 400 eV, which is the recommended value for the employed PAW potentials. In order to sample the Brillouin zone, Monkhorst−Pack grids[58] with a maximum separation of 0.15 $Å^{-1}$ between *k*-points were used throughout the simulations. This grid density, which was found to be enough for convergence of the bulk Ni total energy, corresponds to a $4 \times 4 \times 1$ grid for the reciprocal space of the slab supercell described above. The threshold for forces acting on ions for geometry optimizations was set to 0.01 eV $Å^{-1}$. In order to compensate for the use of an asymmetric slab, all simulations included a dipole correction, as implemented in VASP, based on a method proposed by Makov and Payne.[59]

The configurational space of adsorption was explored by systematically positioning the molecule at different configurations with respect to the surface and performing energy relaxations. For each final stable adsorption configuration, we calculated the adsorption energy E_{ads}^{DFT} as follows

$$E_{ads}^{DFT} = E_{slab+molecule} - (E_{slab} + E_{molecule})$$

where $E_{slab+molecule}$ is the energy of the optimized substrate−adsorbate system, E_{slab} denotes the energy of the relaxed clean Ni{100} surface, and $E_{molecule}$ corresponds to the energy of the Asp molecule in the gas phase at the lowest-energy configuration. In the calculation of dissociative adsorption configurations, where the adsorbate is deprotonated, the protons are adsorbed elsewhere on the metal surface, as far as possible from the Asp molecule.

We also estimated the effect of vibrational zero-point energy (ZPE) on the adsorption energy of some configurations by calculating the vibrational frequencies of the adsorbed molecule (freezing the atoms of the substrate at the relaxed geometry) and the frequencies of the gas-phase molecule. The ZPE values, that is, half the sum of the vibrational frequencies in each case, were then added to the energies $E_{slab+molecule}$ and $E_{molecule}$, in the equation above. This approach assumes that molecular adsorption does not significantly alter the vibrational modes of the much heavier metal atoms on the surface.

For a direct comparison with XPS data, we calculated core-level shifts in the so-called final-state approximation,[60] where the shifts are obtained as total energy differences between two separate calculations, as reported in ref 61. Previous work has shown that this theoretical approach yields relative core-level shifts in excellent agreement with experimental data, including in the case of molecules adsorbed on metal surfaces.[61−65] The method, however, does not yield correct absolute values for the core-level BEs;[61] therefore, we consider core-level shifts, $\Delta BE_{CL}(A)$, instead. Such shifts are defined as the difference in BE of specific core-electrons BE_{CL} between an atom A and a reference atom A_{ref}

$$\Delta BE_{CL}(A) = BE_{CL}(A) - BE_{CL}(A_{ref})$$

We focus our discussion on the relative shifts of the O 1s levels of the oxygen atoms within the Asp molecule. In our previous studies of the MAA/Ni interface, the comparison of the simulated O 1s core levels with experimental XPS allowed us to identify the adsorption geometries.[17,18] Here, we chose the reference atom as the one yielding the lowest O 1s BE. In order to allow a visual comparison between experimental and theoretical data, spectra were modeled by sums of Gaussian peaks with equal width [full width at half-maximum (fwhm) = 1.25 eV, estimated from experimental data] and area, centered at the respective BE shifts. N 1s spectra are not modeled as there is only one N atom in Asp and our method is not capable of accurately predicting absolute BEs. C 1s spectra are not modeled either because carbon atoms are not involved in the surface bonds, and therefore, we do not expect significant differences in C 1s peaks between different adsorption geometries.

RESULTS AND DISCUSSION

XPS Results. XPS spectra of the C 1s, N 1s, and O 1s regions are presented in Figure 1. They are compatible with spectra reported by Karagoz et al. for Asp on Cu{100}[40] and spectra for other amino acids on transition metal surfaces.[15,16,32−39] Spectra were recorded after successively dosing Asp in 5 min intervals (only a selection is shown in the figure) onto the Ni{100} surface held at 250 K. The C 1s and O 1s spectra of the "clean" surface before the first dosing cycle show significant signals (peak "A" in Figure 1a,c) because of carbon segregating from the bulk and carbon/oxygen from dissociating residual gas molecules, such as water and carbon monoxide. After an accumulated dosing time of 30 min, the N 1s spectra, in Figure 1b, changed significantly, with a new peak ("C") appearing at a BE of 402 eV, which is associated with zwitterionic Asp in the second layer. Based on these spectra, we can clearly identify a low coverage regime up to the formation of a single chemisorbed layer (30 min dosing) and a high coverage regime where Asp molecules adsorb on top of the chemisorbed layer. Our DFT calculations (see below) predict that chemisorbed Asp adsorbs in a pentadentate configuration which blocks at least eight Ni atoms. Therefore, one expects the saturated chemisorbed layer to correspond to Θ_{Asp} = 0.125 ML (the coverage Θ_{Asp} is subsequently expressed in terms of Asp molecules per surface Ni atom). By comparing the O 1s peak area of the 30 min layer with that of CO adsorbed to saturation at 250 K on the same surface ($\Theta_{CO} \approx$ 0.35 ML, estimating the reduced coverage due to C contamination from ref 66), the coverage of oxygen atoms was determined as 0.7 ML, which equates to Θ_{Asp} = 0.18 ML (four oxygen atoms per Asp molecule). However, with low photon/kinetic energies of 110−120 eV, as used for collecting the data in Figure 1, photoelectron diffraction can lead to variations in peak intensities which are not proportional to the surface coverage. Therefore, we assume the coverage of the 30 min layer to be 0.125 ML; consequently, the coverages for the higher dosing times are between Θ_{Asp} = 0.17 ML (45 min) and Θ_{Asp} = 0.32 ML (150 min), based on the O 1s signal.

https://dx.doi.org/10.1021/acs.langmuir.0c01175
Langmuir XXXX, XXX, XXX−XXX

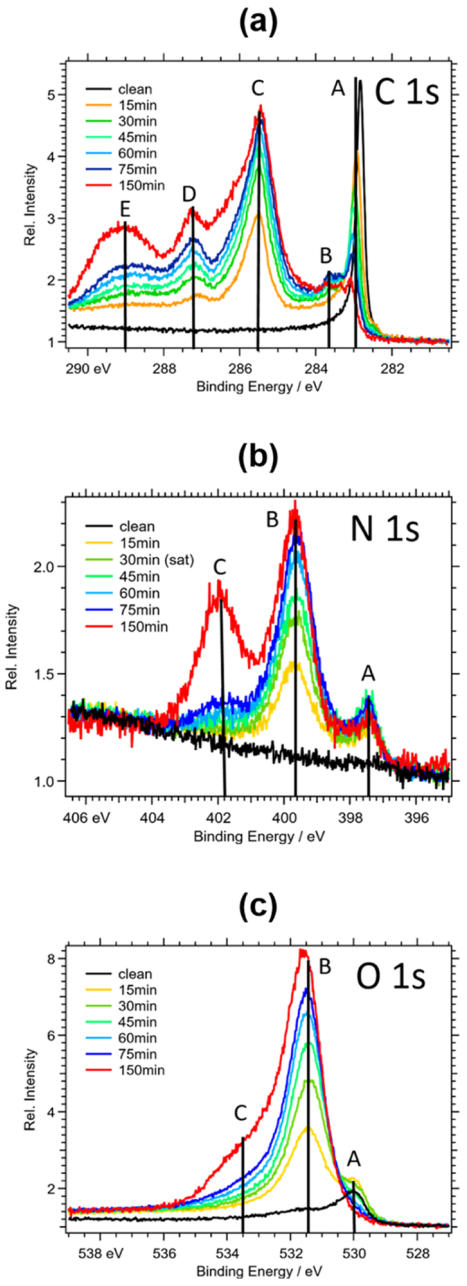

Figure 1. XPS spectra of the (a) C 1s, (b) N 1s, and (c) O 1s regions of Asp adsorbed on Ni{100} at 250 K and at different coverages. The spectra were recorded using photon energies of 400, 510, and 650 eV, respectively.

The N 1s spectra, in Figure 1b, show three peaks associated with the adsorption of Asp at 250 K, at BEs of 397.4 eV (A), 399.7 eV (B), and 401.8 eV (C). For the clean Ni{100} surface, prior to dosing, no N 1s signal is observed. Based on reported spectra of amino acids on Ni{111},[15,16] peak A is assigned to a H_xCN decomposition species, B to the $-NH_2$ amino group of anionic Asp chemisorbed on the metal surface, and C to the $-NH_3^+$ species of zwitterionic Asp in the second layer (or consecutive layers). Peaks A and B appear together at low coverage with A decreasing when the multilayer starts growing. Peak C becomes visible only after a 45 min dose (Θ_{Asp} = 0.17 ML), indicating that multilayer growth sets in after (near) completion of the chemisorbed layer, as seen previously for alanine on Ni{111} and Pd{111}.[15,16,32]

The O 1s spectra (Figure 1c) also show three peaks associated with different chemical environments of the oxygen atoms. Peak A at a BE of 530.0 eV is observed for the nominally clean surface prior to dosing and originates from strongly bound atomic oxygen species, which can only be removed by annealing to >1000 K, at which temperature significant bulk segregation of carbon is observed. The dominant peak B at a BE of 531.4 eV is associated with deprotonated O−C−O carboxylate groups bound to the Ni surface. This is the only adsorbate-related O 1s signal observed for the chemisorbed layer and clearly indicates that both carboxyl groups are deprotonated and all oxygen atoms form bonds with the surface. This peak, like the corresponding C 1s peak at 285.5 eV, coincides with the BEs of CO on Ni{100}; therefore, a contribution of coadsorbed CO (from residual gas during or after dosing) cannot be excluded. Once multilayer growth sets in (>30 min dosing), a new feature, C, at a BE of 533.5 eV, is observed, which is assigned to the protonated oxygen atoms of carboxylic acid groups, OH−C═O.[15,16] As the coverage increases above that of the chemisorbed layer, peak B carries on increasing and shifts to progressively higher BE, indicating that some of the deprotonated oxygen atoms are decoupled from the Ni surface, as one would expect for multilayers. Interestingly, peak A only starts decreasing once the chemisorbed layer is complete, but does so very rapidly afterward. This could either indicate a reaction between surface oxygen and hydrogen (from the deprotonation of the carboxyl groups) followed by desorption of water or the formation of hydrogen bonds between some of the hydroxyl groups and chemisorbed oxygen atoms, which leads to a shift to higher BEs such that their signal merges with peak A.

In the C 1s region, Figure 1a, we can resolve five peaks at BEs of 282.9−283.0 (A), 283.6 (B), 285.5 (C), 287.2 (D), and 289.0 eV (E). Peak A is observed for the nominally clean surface and is associated with carbidic carbon segregating from the Ni bulk. Peak B is associated with dissociation products of the Asp molecule (H_xCN) and/or subsurface carbon atoms.[15,66] After dosing for 30 min (saturated chemisorbed layer), peak A is reduced by 40% in height and shifted by 0.13 eV, but the integrated area of peaks A and B stays exactly the same (within 1%), which indicates that a significant amount of carbidic carbon has been pushed subsurface as a result of Asp adsorption. Earlier, C + CO coadsorption experiments showed that this process can take place even well below the temperature of our experiment.[66] After dosing for 75 min, peak A decreases in intensity by 70% and shifts by 0.25 eV; the integrated area of peaks A and B is now reduced by 15%, which can be explained mostly by attenuation through the multilayer.

The remaining peaks (C, D, and E) originate from carbon atoms of the intact Asp molecule. The assignment of these peaks is based on previous work on amino acids on Ni and other transition metal surfaces.[15,16,32−39] Peak C at a BE of 285.5 eV exhibits the strongest intensity and grows proportionally to the dosing time of Asp. It is assigned to the backbone carbon atoms C1 and C2 of the Asp molecule (cf. Figure 4). As mentioned before, this peak also coincides with the BE of CO on Ni{100}. Peak D at a BE of 287.3 eV is assigned to the carbon atoms C3 and C4 of the deprotonated α and β carboxyl groups. Peak E at 289.0 eV only starts growing significantly after completion of the chemisorbed layer (dosing time > 30 min). It is therefore assigned to protonated carboxylic acid groups.

https://dx.doi.org/10.1021/acs.langmuir.0c01175
Langmuir XXXX, XXX, XXX−XXX

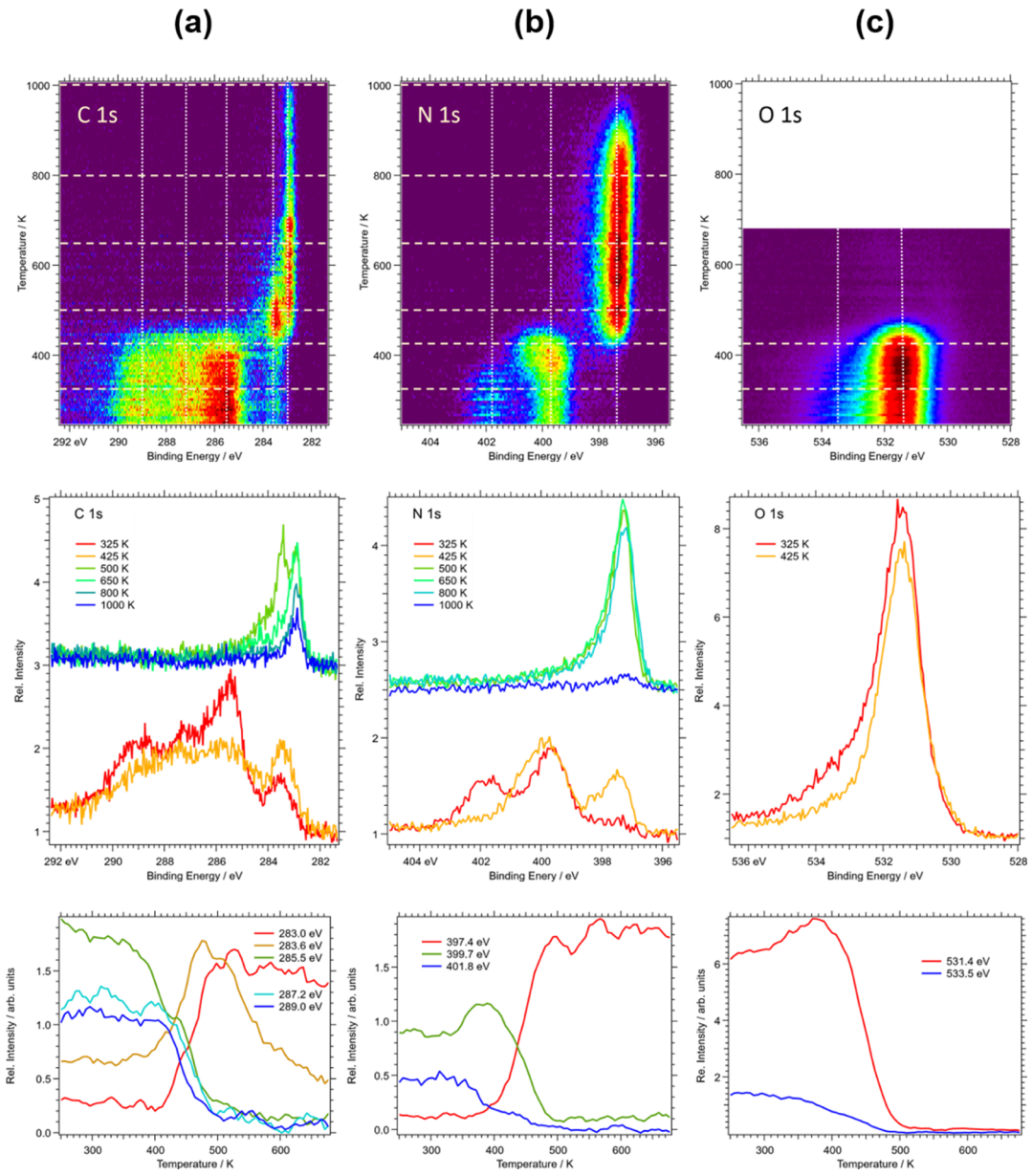

Figure 2. TP-XPS spectra of the (a) C 1s, (b) N 1s, and (c) O 1s regions. Top panels: 2D maps of the XPS intensity vs BE and temperature. Middle panels: selected spectra at key temperatures, 325, 425, 500, 650, 800, and 1000 K (average over two or three spectra within 10 K of specified temperature; the temperatures are indicated in the top panels). Bottom panels: XPS intensity vs temperature for selected BEs (the plotted intensity represents the average over the respective peak width; see the text for more information). The spectra were recorded sequentially with the same photon energy of 650 eV; the heating rate was 5 K min^{-1}, which corresponds to approximately 5.8 K between two spectra of the same region.

Temperature-Programmed XPS. Figure 2 summarizes the TP-XPS experiments by examining the behavior of adsorbed Asp during annealing. The TP-XPS 2D maps (top panels of Figure 2a–c) comprise a series of fast C 1s, N 1s, and O 1s spectra recorded sequentially as the temperature of the sample was increased from 250 to 1000 K at a rate of 5 K min^{-1}. These were merged to produce the 2D plots of temperature versus BE, where the false color scheme indicates the photoelectron intensity. The temperature difference between two spectra of the same kind is approximately 5.8 K. Examples of individual spectra (average over two or three spectra within 10 K of specified temperature) are shown in the middle panels of Figure 2a–c. Prior to the TP-XPS experiments, Asp was deposited onto the Ni{100} surface at 250 K for 150 min to form the multilayer structure, as indicated by a strong N 1s signal at 401.8 eV (cf. peak C in Figure 1b). Vertical line profiles taken at the BEs corresponding to the XPS peaks are shown at the bottom of each column to illustrate the evolution of the chemical species associated with these peaks in the temperature range 250–670 K. The evolution of the multilayer at low temperatures is best observed through the N 1s spectra in Figure 2b. The diagram at the bottom of Figure 2b shows a rapid decrease of peak C (a BE of 401.8, assigned to NH_3^+) between 360 and 400 K, indicating the desorption of molecules adsorbed onto the multilayer. The individual spectrum measured at 325 K (middle panel) shows a well-resolved peak at 401.8 eV, which completely disappears at 425 K. The decomposition of the chemisorbed layer is indicated by a decrease in the N 1s signal at a BE of 399.7 eV (peak B, assigned to NH_2) and an

https://dx.doi.org/10.1021/acs.langmuir.0c01175
Langmuir XXXX, XXX, XXX–XXX

abrupt change in the spectra between 400 and 450 K. In this temperature range, all the remaining N 1s intensity shifts to a peak around BE 397.5 eV, which is associated with atomic nitrogen adsorbed on the Ni surface. This species is very stable; the peak disappears between 860 and 940 K, most likely via desorption of N_2, as in the case of alanine on Ni{111}.[15]

Similarly, dramatic changes in this temperature range are seen in the C 1s and O 1s spectra (Figure 2a,c). The intensities of the high BE C 1s peaks between 285 and 289 eV, which are assigned to the intact molecules, decrease rapidly between 400 and 470 K (Figure 2a, bottom panel). Simultaneously, two peaks (A and B) emerge above 400 K, at BEs of 283.0 and 283.6 eV, respectively. These peaks are associated with dissociation products on the surface and/or subsurface carbidic carbon.[66] Peak B disappears between 520 and 610 K, while no increase is observed in this temperature range at any other BEs of the C 1s signal. Therefore, we associate this with a H_xCN fragment desorbing from the surface. The intensity of peak A at a BE of 283.0 eV gradually decreases with increasing temperature, most likely through diffusion of carbon into the Ni bulk. The associated surface species is most likely atomic carbon as it has been observed on other Ni surfaces after amino acid decomposition under similar conditions (e.g., ref 15). Traces of this species are still observed, even after annealing to 1000 K. Interestingly, the temperature dependence of the carbon-containing decomposition species is not linked to the N 1s signal at 397.4 eV, that is, the corresponding species react independently, which is in contrast to the observations for alanine on Ni{111}.[15]

The main O 1s peak (B) at a BE of 531.4 eV starts to decrease at around 400 K (see Figure 2c, bottom). At 500 K, the O 1s signal is no longer observed, that is, no decomposition products containing oxygen are left on the surface. The slight increase in signal intensity at lower temperatures is similar to the behavior of the N 1s signal at 399.7 eV. This is most likely due to reordering and desorption of molecules from the multilayer, as indicated by the decrease in the signal at 533.5 eV.

In summary, the complete decomposition of chemisorbed Asp is associated with the appearance of the XPS signal assigned to decomposition products in the C 1s and N 1s TP-XPS spectra at BEs of 283.1, 283.6, and 397.5 eV. Above 500 K, no C 1, N 1s, or O 1s XPS signal related to intact chemisorbed Asp is observed. The fact that no oxygen-containing decomposition products are observed on the surface indicates that the dissociation of Asp leads to the formation of CO_2 desorbing from the surface. After the decomposition of Asp, carbon- and nitrogen-containing surface species undergo further transformation upon heating.

NEXAFS and Molecular Orientation. Aspects of the molecular geometry can be derived from the polarization/angular dependence of π-resonance features in X-ray absorption of the oxygen K edge.[18,42] In simple amino acids without additional C═O bonds, these originate from the carboxylate groups; therefore, their angular dependence enables us to determine their orientation with respect to the surface plane. The top panel of Figure 3 shows O K-edge NEXAFS spectra of a saturated chemisorbed layer of Asp on Ni{100} recorded at 250 K. Data were recorded with incidence angles of 0, 35, and 70° with respect to the surface normal, which correspond to angles of 90, 55, and 20° of the X-ray polarization vector. The spectra are dominated by a π-resonance peak around 533 eV, which is preceded by a small

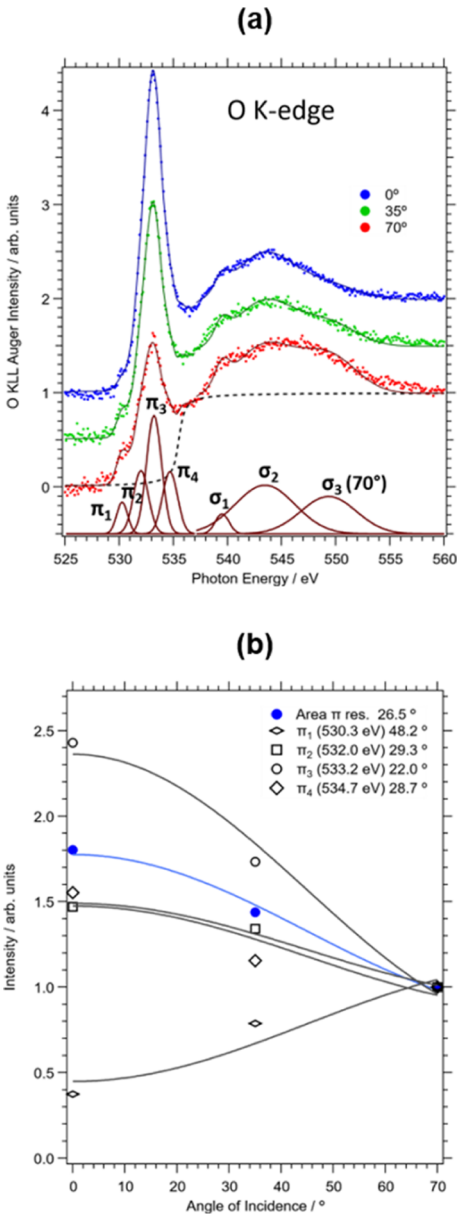

Figure 3. (a) Oxygen K-edge NEXAFS spectra of the saturated chemisorbed Asp layer at 250 K; (b) angular dependence of the peaks constituting the pre-edge π resonance. For easier comparison, the peak intensities in (b) have been normalized with respect to the value at 70°.

shoulder at 530.3 eV (π_1) and three distinguishable broad σ-resonance features at 539.5 eV (σ_1), 543.6 eV (σ_2), and 549.3 eV (σ_3). The latter is attributed to C−C and C−O bonds and the former is attributed to the carboxylate groups, in accordance with the assignments made previously for other amino acids on metal surfaces.[15,28,39] In order to determine their angular dependence, a step function (position 535.4 eV and width 2.0 eV) was subtracted from the data, and the π and σ-resonance regions were fitted separately with Gaussian functions. The individual peaks of the fit for the 70° spectrum are shown at the bottom of Figure 3a. In the following, we will concentrate on the π-resonance features. To obtain good agreement with the experimental data, the main peak had to be fitted with three Gaussians, π_2 (532.0 eV), π_3 (533.2 eV), and π_4 (534.7 eV), each with an fwhm of 1.6 eV. The angular

https://dx.doi.org/10.1021/acs.langmuir.0c01175
Langmuir XXXX, XXX, XXX−XXX

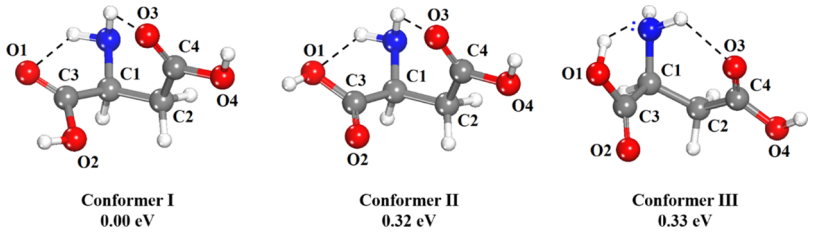

Figure 4. Molecular structure of the lowest-energy conformers of gaseous Asp, according to DFT modeling. See Table S1 of the Supporting Information for numerical values of bond length and angles. The relative stability is in line with previous studies at B3LYP, MP2, and CCSD levels, as reported in ref 67.

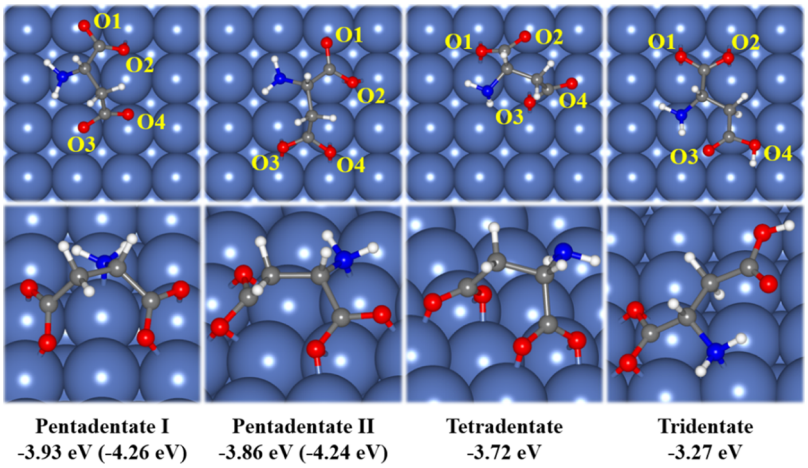

Figure 5. Lowest-energy configurations of adsorption of Asp on the Ni{100} surface, according to DFT simulations. Values in brackets include vibrational contributions. Oxygen atoms are numbered in line with Figure 4 and with the discussion of core-level shifts below. See Table S2 of the Supporting Information for numerical values of bond length and angles.

dependence of their intensities is plotted in Figure 3b, alongside the angular dependence of π_1 and the area of the entire π resonance feature (integrated between 527 and 536 eV). Figure 3b also includes fits to each of the data sets using a modified version of the formula given by Stöhr[42] for fourfold symmetric substrates

$$I(\theta) = A\left[P(\sin\theta)^2\left(1 - \frac{3}{2}(\sin\gamma)^2\right) + \frac{1}{2}(\sin\gamma)^2\right]$$

where θ is the polar angle of incidence (with respect to the surface normal) and γ is the tilt angle of the O−C−O plane of the carboxylate group with respect to the surface plane (∠O−C−O). Here, we are assuming that both carboxylate groups in the adsorbed Asp molecule have the same tilt angle. The results of these fits lead to tilt angles between ∠O−C−O = 22.0 and 29.3° for the main π-resonance (the individual values are listed in the legend of Figure 3b) and 48.2° for the small π_1 feature at 530.3 eV. As the area of the latter peak is on average only about 5% of the main resonance, it must originate from a minority species, so we conclude that the O−C−O tilt angle of the majority of chemisorbed Asp molecules on Ni{100} is 26 ± 4°.

DFT Simulation of Asp in the Gas Phase. In order to calculate adsorption energies, we must obtain the energy of Asp in the gas phase as a reference. As shown in Figure 4, Asp has three functional groups: α-amino group (α-NH_2), α-carboxyl group (α-COOH), and β-carboxyl group (β-COOH). Relative rotation of the functional groups results in different conformations. A systematic conformational search of the molecular geometry in the gas phase and in solution has been previously performed by Chen and Lin[67] using B3LYP, MP2, and CCSD levels of theory. Given the combinations of the internal single-bond rotamers, a total of 1296 trial canonical structures and 216 trial zwitterionic structures were generated for the Asp molecule. Of these, 139 canonical conformers were found to be stable in the gas phase; it was found that zwitterionic structures were not stable in the gas phase.

We selected the three lowest-energy conformers of Asp in the gas phase, according to their relative CCSD-level energies in this study, to be calculated with our computational setup. Spatial configurations after optimization are displayed in Figure 4. The presence of linked hydrogen bonds due to the interaction of the amino group with the carboxylic groups increases the stability of the conformers. The maximum stability is achieved when the two amino hydrogen atoms interact with the carbonyl oxygen of the two carboxylic groups: the repulsive interaction of the protons promotes NH_2···O hydrogen bonding (conformer I). The stability is reduced by 0.32 eV when one of the NH_2···O hydrogen bonds is promoted by the hydroxyl of the α-COOH group via the oxygen atom (conformer II). A similar decrease in energy of 0.33 eV is observed when the lone pair of the amino interacts with the proton of the hydroxyl in the α-COOH group; in this case, one amino hydrogen is repelled, whereas the other interacts with the carbonyl oxygen of the β-COOH group, promoting a single NH_2···O hydrogen bonding (conformer III). Overall, judged by the average distance between C3 and C4 whose values range from 3.05 to 3.11 Å, the direct interaction of the NH_2 group with the COOH groups results in a compact structure.

https://dx.doi.org/10.1021/acs.langmuir.0c01175
Langmuir XXXX, XXX, XXX−XXX

Table 1. Key Geometrical and Spectroscopic Parameters of the Two Lowest-Energy Candidates Found by DFT Simulations[a,b]

	pentadentate I	pentadentate II	tetradentate	tridentate
E_{ads}^{DFT}	−3.93 eV	−3.86 eV	−3.72 eV	−3.27 eV
$E_{ads}^{DFT+ZPE}$	−4.26 eV	−4.24 eV		
d(O1−Ni)	2.017 Å	1.968 Å	2.027 Å/2.174 Å	2.098 Å/2.000 Å
d(O2−Ni)	2.066 Å	2.060 Å/2.111 Å	1.975 Å	2.138 Å/1.999 Å
d(O3−Ni)	2.006 Å	1.968 Å/2.159 Å	2.124 Å/2.050 Å	
d(O4−Ni)	1.950 Å	1.995 Å/2.012 Å	1.980 Å	
d(N−Ni)	2.090 Å	2.019 Å		2.045 Å
∠O1−C−O2-surface	38.8°	15.7°	56.6°	13.5°
∠O3−C−O4-surface	54.0°	20.2°	68.5°	27.2°
Δz(C)	1.27 Å	1.11 Å	1.38 Å	1.78 Å
ΔBE (O1)	0.00 eV	0.00 eV	0.21 eV	0.03 eV
ΔBE (O2)	0.31 eV	0.28 eV	0.02 eV	0.00 eV
ΔBE (O3)	0.13 eV	0.43 eV	0.18 eV	0.49 eV
ΔBE (O4)	0.30 eV	0.58 eV	0.00 eV	3.08 eV

[a]See Table S2 of the Supporting Information for additional numerical values of bond length and angles. [b]Δz(C) is the maximum vertical height difference of the molecule's carbon atoms.

Although our computed relative energies are larger than the relative energies at the CCSD level reported in ref 67, the order of stability is the same as in that study. Conformer I is the most stable configuration of Asp in the gas phase, so we use it here as the reference for the calculation of adsorption energies. In any case, the selection of reference is largely arbitrary as our focus is the relative stability of the different adsorption configurations.

DFT Simulation of Asp Adsorption on Ni{100}. In the exploration of adsorption geometries, we have considered penta-, tetra-, tri-, and bidentate modes of adsorption of anionic Asp over Ni{100} surfaces. The optimized geometries after relaxation are shown in Figure 5. In the pentadentate configurations, all oxygen and nitrogen atoms of the doubly-deprotonated Asp molecule form bonds with the Ni surface. We obtained two possible candidates with this coordination: in the "pentadentate I" configuration, all interacting atoms of the adsorbate are on atop sites, whereas the two dissociated hydrogen atoms are adsorbed elsewhere on the Ni surface on four-hollow sites. The planes of the α-carboxyl group and that of the β-carboxyl group form angles with the metal surface of ∠O1−C−O2 = 38.8° and ∠O3−C−O4 = 54.0°, respectively. The anionic Asp is accommodated over six Ni surface atoms, resulting in a compact structure. In the "pentadentate II" configuration, the deprotonated adsorbate is more spread and covers eight surface Ni atoms. The angles between the Ni surface and the planes of the α-carboxyl group and β-carboxyl group were computed as ∠O1−C−O2 = 15.7° and ∠O3−C−O4 = 20.2°, respectively. Three oxygen atoms (O2, O3, and O4) are located on bridge sites, while the remaining oxygen atom (O1) and the amino nitrogen are located on atop sites. In the "tetradentate" structure, the nitrogen-surface bond is missing and only the oxygen atoms take part in the adsorbate-surface bonding: two oxygen atoms (O1 and O3) are on bridge sites and the other two (O2 and O4) are on atop sites. The two dissociated hydrogen atoms occupy four-hollow sites on the Ni surface. In this geometry, the tilt angles of the carboxylic groups were computed as 56.6 and 68.5° for the α-carboxyl group and β-carboxyl group, respectively. Finally, in the "tridentate" geometry, only the α-NH_2 group and the α-COOH group have direct interactions with the Ni surface. The nitrogen atom is on an atop site, and the two oxygen atoms (O1 and O2) are on bridge sites. The dissociated hydrogen sits on a four-hollow site. The angle between the α-carboxyl group and the Ni surface is 13.5°. We also tried a bidentate start configuration for the dissociative adsorption of Asp, but it converged to a tridentate configuration after geometry optimization.

The calculated adsorption energies without vibrational contributions are −3.93, −3.86, −3.72, and −3.27 eV for the "pentadentate I," "pentadentate II," "tetradentate," and "tridentate" configurations, respectively. Therefore, the pentadentate modes of adsorption are clearly favored over the other coordinations. The two pentadentate configurations have very similar adsorption energies. In an attempt to make a more accurate energy comparison between the two candidates, we included the vibrational contributions, in the form of ZPE corrections, in the computed adsorption energies. The ZPE stabilizes the pentadentate I configuration by −0.32 eV and the pentadentate II configuration by −0.38 eV. The corrected adsorption energies are therefore −4.26 eV for the pentadentate I configuration and −4.24 eV for the pentadentate II. This adsorption energy difference is not significant, given the general precision of DFT calculations and the approximations involved in our models.

Although the calculations suggest that pentadentate configurations are the most favorable, the small differences in adsorption energies do not allow an unambiguous discrimination between them on the basis of adsorption energies alone. Furthermore, all the configurations feature very negative adsorption energies and could therefore represent local minima in the potential energy landscape, with high transition barriers between them, which might allow them to coexist. Consequently, we need to resort to a combined analysis of the experimental XPS and NEXAFS data and the DFT-calculated geometric and spectroscopic properties in order to make a reliable determination of the adsorption complex.

Combined Assessment of Theoretical and Experimental Spectroscopic Data. Table 1 lists key geometric parameters of the four adsorption structures described above, as calculated from DFT, together with the predicted relative chemical shifts in the O 1s BEs. These were used to model O 1s XPS spectra through a superposition of Gaussian peaks (an fwhm of 1.25 eV) with the respective energy separations. They are shown in Figure 6 together with the experimental data of a saturated chemisorbed layer. This approach assumes that the

https://dx.doi.org/10.1021/acs.langmuir.0c01175
Langmuir XXXX, XXX, XXX−XXX

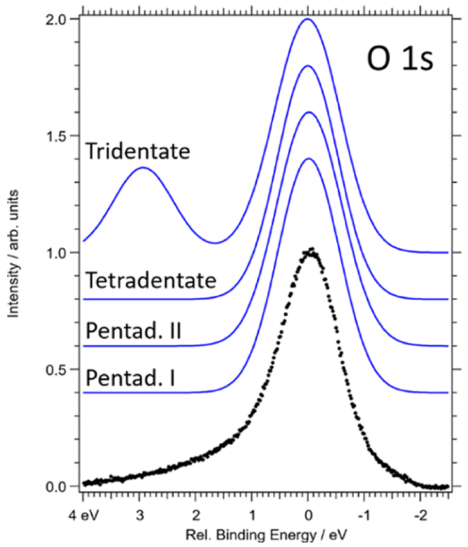

Figure 6. Comparison of modeled O 1s XPS spectra with the experimental data for a saturated chemisorbed layer of Asp on Ni{100}. Spectra are normalized with respect to the highest intensity, and the energy axes are aligned such that the position of the highest peak is at 0 eV.

photoemission yield is proportional to the number of atoms and is not affected by photoelectron diffraction or other nonlinear effects. Nevertheless, tridentate adsorption can clearly be excluded as it would lead to an extra peak at high BEs, which is associated with the protonated oxygen atom O4 of the β-carboxyl group. The other three adsorption geometries, pentadentate I/II and tetradentate, lead to a reasonably good agreement with the experimental data.

In addition to the XPS BEs, the O−C−O tilt angle determined by NEXAFS is another parameter enabling us to distinguish between the candidate geometries. Of the three geometries that are compatible with the XPS data, only the pentadentate II model features tilt angles which are similar to those determined by NEXAFS, 15.7 and 20.2° versus 26 ± 4°. The values of the other two models, ranging between 38.5 and 68.5°, are significantly less compatible with the NEXAFS data. Here, we should note that the tilt angles of the tridentate adsorption geometry are also compatible with NEXAFS, but, as shown above, this model is not compatible with XPS and is also the least favored in terms of calculated adsorption energies (~0.6 eV higher than that for the pentadentate geometries). In summary, from this combined analysis, only the "pentadentate II" model is compatible with all our spectroscopic and calculated data.

The discrepancy between the tilt angle derived from the angular dependency of the π resonance peak in O K edge NEXAFS and the tilt angles in the pentadentate DFT geometry is most likely due to systematic and statistical errors of both the experiment and the modeling involved. In this context, it is important to note that the analysis of the experimental data assumes a local mirror symmetry with respect to the O−C−O planes of the carboxylate groups. This symmetry is clearly broken by the proximity of the Ni surface on one side of the plane, and consequently, the orbital into which the O 1s electron is excited is distorted compared to a gas-phase-like π-orbital. This can be seen clearly from the charge density isosurfaces in the upper panel of Figure 7, where the related π-orbitals of the pentadentate II structure have more of their weight below the O−C−O planes than above. A comparison with the pentadentate I structure, which has less acute tilt angles, shows that this leads to more symmetric shape of the π orbitals.

Based on their STM and IR spectroscopy data for Asp on Ni{111}, Wilson et al. concluded that a polycondensation reaction takes place at low coverage, leading to the formation of polysuccinimide, $[C_4H_3NO_2]_n$.[21] We can exclude this for Ni{100} on the basis of our XPS and NEXAFS results, as surface bonds of all N and O atoms (as evident from XPS) in

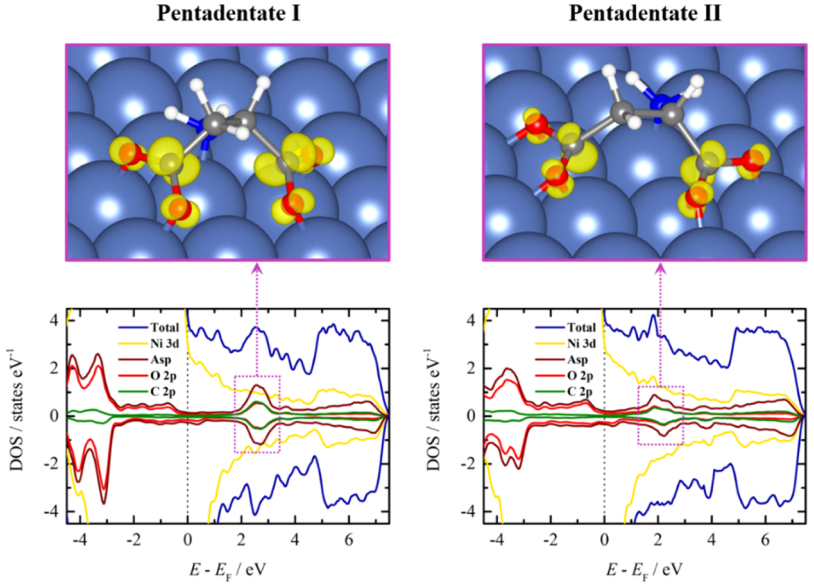

Figure 7. Electronic density of states of the two lowest-energy configurations predicted by DFT (bottom). The vertical dashed line marks the Fermi level (E_F). The charge density isosurfaces (top), corresponding to electronic states with energies between 1.92 and 3.32 eV (for the "pentadentate I" candidate) and 1.26 and 2.86 eV (for the "pentadentate II" geometry) above the Fermi level, are highlighted with dotted rectangles.

https://dx.doi.org/10.1021/acs.langmuir.0c01175
Langmuir XXXX, XXX, XXX−XXX

polysuccinimide would lead to C═O bonds parallel to the surface, which is incompatible with our NEXAFS data.

The adsorption complex, as depicted in Figure 5, shows relatively little distortion with respect to the gas-phase geometry of Asp (see Tables S1 and S2 in the Supporting Information). The molecule binds to eight Ni surface atoms and shows strong chiral asymmetry, with the carboxylate and amino groups exposed such that they can form hydrogen bonds with other adsorbed organic molecules. It is therefore plausible that Asp will strongly interact with reactants of hydrogenation reactions, such as MAA, and thus act as a chiral modifier. We cannot comment on the details of this interaction in the absence of coadsorption studies, but comparing the ZPE-corrected adsorption energies of MAA (−2.02 eV)[18] and Asp (−4.24 eV) on Ni{100}, it is clear that Asp is more firmly anchored to the surface. This is not surprising as Asp makes five covalent bonds with the surface as opposed to two in the case of MAA. One can therefore expect that Asp will stereodirect the more weakly bound MAA rather than vice versa.

Not only is Asp bound very strongly to the surface but it is also significantly more stable than smaller adsorbates, such as MAA or Ala, on Ni single-crystal surfaces. The reported decomposition temperatures for these molecules range from 300 to 350 K,[15,16,18] whereas Asp on Ni{100} starts decomposing at around 400 K. This temperature is also higher than the onset of decomposition for Asp on Ni{111}, which Wilson et al. reported at around 350 K.[21] The thermal stability of the molecule is not directly linked to its adsorption energy. The reason for the high stability of Asp on Ni{100} probably lies in the relatively undistorted molecular geometry compared to the gas phase (see Tables S1 and S2 in the Supporting Information).

Our calculations were performed for a low coverage of Asp, for which there is no hydrogen bonding interaction with neighboring molecules. Hydrogen bonding is very likely at higher coverage as this is observed for the most smaller amino acids adsorbed on metal surfaces.[15,16,22,23,32−37] The effect would most likely be a further increase in the adsorption energy of typically 0.25 eV per hydrogen bond.[22] Because we do not have any experimental information about the lateral arrangement and/or long-range order of Asp molecules on the Ni{100} surface, the number of possible configurations with lateral interactions would be too large to sample by DFT. However, on the basis of our XPS data, we can exclude a reduction in the number of molecule-surface bonds induced by hydrogen bonding as this would lead to additional peaks in the O 1s spectrum (see Figure 6) and/or a shift in the N 1s spectrum to higher BE.

Finally, we theoretically consider whether under the hydrogen-rich conditions of hydrogenation reactions (hydrogen partial pressures of up to ∼100 bar),[2,3,6,7] the adsorbed pentadentate Asp species could gain hydrogen. With this purpose, we calculate the "hydrogenation energy" (ΔE_{hyd}) required to form adsorbed tetradentate zwitterionic species (i.e., with the N losing the coordination to the surface and forming NH_3, similarly to what has been observed for alanine at high coverage on Ni and Pd surfaces).[15,16,24,32] With reference to an isolated H_2 molecule in the gas phase and including ZPE corrections, we obtain ΔE_{hyd} = 0.37 eV, which indicates that the hydrogenation process is endothermic. Whether the process is thermodynamically favorable or not depends on the specific conditions of temperature (T) and partial pressure of hydrogen (p_{H_2}). Assuming that T and p_{H_2} affect the reaction free energy (ΔG_{hyd}) only via the free energy of the gas phase (which is a typical approximation in ab initio thermodynamics),[68] we obtain

$$\Delta G_{hyd} = \Delta E_{hyd} - \frac{1}{2}\mu_{H_2}(p_{H_2}, T)$$

where μ_{H_2} is the chemical potential of hydrogen gas with respect to an isolated H_2 molecule, taken from thermodynamic tables.[69] The equation mentioned above is plotted in Figure 8,

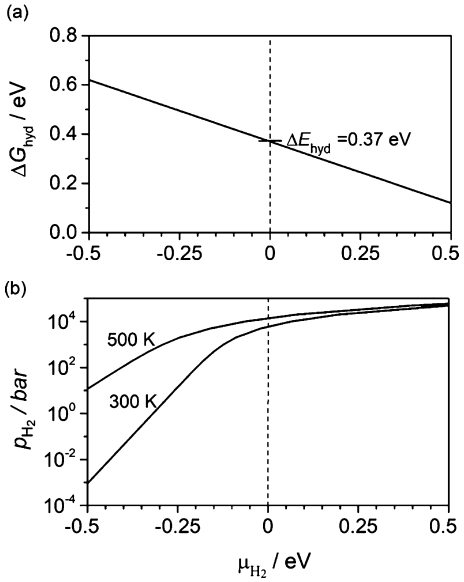

Figure 8. (a) Free energy change involved in hydrogenating an Asp species adsorbed in pentadentate configuration on the Ni{100} surface to form a zwitterionic species adsorbed in tetradentate configuration, from hydrogen in the gas phase, as a function of molecular hydrogen chemical potential; (b) hydrogen partial pressures required to achieve these chemical potentials at 300 and 500 K.

in a range of chemical potentials, together with the hydrogen partial pressures required to achieve these chemical potentials at 300 or 500 K. The hydrogenation of the adsorbed Asp species to form a NH_3 group is unfavorable ($\Delta G_{hyd} > 0$) in the presence of hydrogen gas, even at hydrogen partial pressures of the order 10^4 bar. Although actual reaction conditions are more complicated (e.g., reactions happen in the liquid phase, with hydrogen dissolved in a solvent such as water or an alcohol), the present analysis suggests that the preferred modes of adsorption found in this work would not be affected by hydrogen-rich conditions.

CONCLUSIONS

The combination of experimental XPS and NEXAFS studies and theoretical modeling shows that the dominant mode of adsorption of Asp on Ni{100} surfaces is a pentadentate configuration, where three oxygen atoms are bonded to the surface on bridge sites, while the remaining oxygen atom and the amino nitrogen are located on atop sites. Only this configuration is found to be compatible with all experimental spectroscopic data. Other pentadentate and tetradentate configurations lead to similar adsorption energies and would be compatible with the XPS data, but they involve molecular

https://dx.doi.org/10.1021/acs.langmuir.0c01175
Langmuir XXXX, XXX, XXX−XXX

orientations which are not compatible with the NEXAFS data. Because of the high surface coordination and an adsorption geometry which only involves minor distortions from the gas-phase molecular geometry, chemisorbed Asp shows remarkable thermal stability with no signs of decomposition up to 400 K. During the adsorption process, surface carbon appears to be dissolved into the nickel bulk, which is most likely another consequence of the strong surface bond of Asp. The combined analysis of experimental measurements and DFT simulations allows us to unambiguously identify the preferred mode of adsorption. Understanding the interaction of Asp with nickel surfaces gives insights into its role as a chiral modifier of Ni-based catalysts for enantioselective hydrogenation reactions.

■ ASSOCIATED CONTENT

Supporting Information

The Supporting Information is available free of charge at https://pubs.acs.org/doi/10.1021/acs.langmuir.0c01175.

Additional data from DFT calculations: geometrical properties of gas-phase aspartic acid, geometrical properties of adsorbed aspartic acid on Ni{100}, and vibrational frequencies for adsorbed aspartic acid on Ni{100} (PDF)

■ AUTHOR INFORMATION

Corresponding Authors

Ricardo Grau-Crespo − *Department of Chemistry, University of Reading, Reading RG6 6AD, U.K.;* orcid.org/0000-0001-8845-1719; Email: r.grau-crespo@reading.ac.uk

Georg Held − *Diamond Light Source Harwell Science and Innovation Campus, Didcot OX11 0QX, U.K.;* orcid.org/0000-0003-0726-4183; Email: georg.held@diamond.ac.uk

Authors

Wilson Quevedo − *Diamond Light Source Harwell Science and Innovation Campus, Didcot OX11 0QX, U.K.*

Jorge Ontaneda − *Departamento de Química, Universidad Técnica Particular de Loja, Loja 1101608, Ecuador;* orcid.org/0000-0003-1538-365X

Alexander Large − *Department of Chemistry, University of Reading, Reading RG6 6AD, U.K.*

Jake M. Seymour − *Department of Chemistry, University of Reading, Reading RG6 6AD, U.K.*

Roger A. Bennett − *Department of Chemistry, University of Reading, Reading RG6 6AD, U.K.;* orcid.org/0000-0001-6266-3510

Complete contact information is available at: https://pubs.acs.org/10.1021/acs.langmuir.0c01175

Notes

The authors declare no competing financial interest.

■ ACKNOWLEDGMENTS

This work made use of ARCHER, the UK's national high-performance computing service, via the UK's HPC Materials Chemistry Consortium, which is funded by EPSRC (EP/R029431). A.L. acknowledges part funding for a studentship from Johnson Matthey plc. The beamtime at Elettra—Sincrotrone Trieste (proposal no. 20180430) leading to this work has been supported by the project CALIPSOplus under grant agreement 730872 from the EU Framework Programme for Research and Innovation HORIZON 2020. The authors thank the staff of Elettra for their help during the experiments, in particular, Silvano Lizzit, Paolo Lacovig, and Daniel Lizzit.

■ REFERENCES

(1) Sharpless, K. B. Searching for New Reactivity (Nobel Lecture). *Angew. Chem., Int. Ed.* **2002**, *41*, 2024−2032.

(2) Fukawa, H.; Izumi, Y.; Komatsu, S.; Akabori, S. Studies on Modified Hydrogenation Catalyst. I. Selective Hydrogenation Activity of Modified Raney Nickel Catalyst for Carbonyl Group and C=C Double Bond. *Bull. Chem. Soc. Jpn.* **1962**, *35*, 1703−1706.

(3) Izumi, Y. Modified Raney Nickel (MRNi) Catalyst: Heterogeneous Enantio-Differentiating (Asymmetric) Catalyst. *Adv. Catal.* **1983**, *32*, 215−271.

(4) Baddeley, C. J.; Jones, T. E.; Trant, A. G.; Wilson, K. E. Fundamental Investigations of Enantioselective Heterogeneous Catalysis. *Top. Catal.* **2011**, *54*, 1348−1356.

(5) Baddeley, C. J.; Held, G. Chiral Molecules on Surfaces. *Comprehensive Nanoscience and Technology*; Elsevier Inc., 2011; Vol. *1*−*5*, pp 105−133.

(6) Keane, M. A. Adsorption of Optically Pure Alanine on Silica-Supported Nickel and the Consequent Catalytic Enantioselectivity. *Langmuir* **1994**, *10*, 4560−4565.

(7) Keane, M. A. Interaction of Optically Active Tartaric Acid with a Nickel−Silica Catalyst: Role of Both the Modification and Reaction Media in Determining Enantioselectivity. *Langmuir* **1997**, *13*, 41−50.

(8) Jones, T. E.; Rekatas, A. E.; Baddeley, C. J. Influence of Modification PH and Temperature on the Interaction of Methyl-acetoacetate with (S)-Glutamic Acid-Modified Ni{111}. *J. Phys. Chem. C* **2007**, *111*, 5500−5505.

(9) Wilson, K. E.; Baddeley, C. J. Understanding the Surface Chemistry of Enantioselective Heterogeneous Reactions: Influence of Modification Variables on the Interaction of Methylacetoacetate with (S)-Aspartic Acid Modified Ni{111}. *J. Phys. Chem. C* **2009**, *113*, 10706−10711.

(10) Jones, T. E.; Baddeley, C. J. A RAIRS, STM and TPD Study of the Ni{111}/R,R-Tartaric Acid System: Modelling the Chiral Modification of Ni Nanoparticles. *Surf. Sci.* **2002**, *513*, 453−467.

(11) Jones, T. E.; Baddeley, C. J. An Investigation of the Adsorption of (R,R)-Tartaric Acid on Oxidised Ni{111} Surfaces. *J. Mol. Catal. A: Chem.* **2004**, *216*, 223−231.

(12) Humblot, V.; Haq, S.; Muryn, C.; Hofer, W. A.; Raval, R. From Local Adsorption Stresses to Chiral Surfaces: (R,R)-Tartaric Acid on Ni(110). *J. Am. Chem. Soc.* **2002**, *124*, 503−510.

(13) Humblot, V.; Haq, S.; Muryn, C.; Raval, R. (R,R)-Tartaric Acid on Ni(110): The Dynamic Nature of Chiral Adsorption Motifs. *J. Catal.* **2004**, *228*, 130−140.

(14) Jones, T. E.; Urquhart, M. E.; Baddeley, C. J. An Investigation of the Influence of Temperature on the Adsorption of the Chiral Modifier, (S)-Glutamic Acid, on Ni{111}. *Surf. Sci.* **2005**, *587*, 69−77.

(15) Nicklin, R. E. J.; Cornish, A.; Shavorskiy, A.; Baldanza, S.; Schulte, K.; Liu, Z.; Bennett, R. A.; Held, G. Surface Chemistry of Alanine on Ni{111}. *J. Phys. Chem. C* **2015**, *119*, 26566−26574.

(16) Nicklin, R. E. J.; Shavorskiy, A.; Aksoy Akgul, F.; Liu, Z.; Bennett, R. A.; Sacchi, M.; Held, G. "Pop-On and Pop-Off" Surface Chemistry of Alanine on Ni{111} under Elevated Hydrogen Pressures. *J. Phys. Chem. C* **2018**, *122*, 7720−7730.

(17) Ontaneda, J.; Nicklin, R. E. J.; Cornish, A.; Roldan, A.; Grau-Crespo, R.; Held, G. Adsorption of Methyl Acetoacetate at Ni{111}: Experiment and Theory. *J. Phys. Chem. C* **2016**, *120*, 27490−27499.

(18) Tsaousis, P.; Ontaneda, J.; Bignardi, L.; Bennett, R. A.; Grau-Crespo, R.; Held, G. Combined Experimental and Theoretical Study of Methyl Acetoacetate Adsorption on Ni{100}. *J. Phys. Chem. C* **2018**, *122*, 6186−6194.

(19) Jones, T. E.; Baddeley, C. J. Direct STM Evidence of a Surface Interaction between Chiral Modifier and Pro-Chiral Reagent: Methylacetoacetate on R,R-Tartaric Acid Modified Ni{111}. *Surf. Sci.* **2002**, *519*, 237−249.

(20) Jones, T. E.; Baddeley, C. J. Investigating the Mechanism of Chiral Surface Reactions: The Interaction of Methylacetoacetate with (S)-Glutamic Acid Modified Ni{111}. *Langmuir* **2006**, *22*, 148−152.
(21) Wilson, K. E.; Trant, A. G.; Baddeley, C. J. Interaction of the Pro-Chiral Molecule, Methylacetoacetate, with (S)-Aspartic Acid Modified Ni{111}. *J. Phys. Chem. C* **2012**, *116*, 1092−1098.
(22) Jones, G.; Jenkins, S. J.; King, D. A. Hydrogen Bonds at Metal Surfaces: Universal Scaling and Quantification of Substrate Effects. *Surf. Sci.* **2006**, *600*, 224−228.
(23) Zheleva, Z. V.; Eralp, T.; Held, G. Complete Experimental Structure Determination of the p(3 × 2)Pg Phase of Glycine on Cu{110}. *J. Phys. Chem. C* **2012**, *116*, 618−625.
(24) Burkholder, L.; Chamberlin, S. E.; Kraffczyk, H.; Michels, M.; Boscoboinik, A.; Adams, H.; Hopper, N.; Held, G.; Hirschmugl, C.; Tysoe, W. T. The Structure of Alanine Anionic-Zwitterionic Dimers on Pd(111); Formation of Salt Bridges. *Surf. Sci.* **2019**, *679*, 79−85.
(25) Efstathiou, V.; Woodruff, D. P. Characterisation of the Interaction of Glycine with Cu(1 0 0) and Cu(1 1 1). *Surf. Sci.* **2003**, *531*, 304−318.
(26) Sayago, D. I.; Polcik, M.; Nisbet, G.; Lamont, C. L. A.; Woodruff, D. P. Local Structure Determination of a Chiral Adsorbate: Alanine on Cu(1 1 0). *Surf. Sci.* **2005**, *590*, 76−87.
(27) Kang, J.-H.; Toomes, R. L.; Polcik, M.; Kittel, M.; Hoeft, J.-T.; Efstathiou, V.; Woodruff, D. P.; Bradshaw, A. M. Structural Investigation of Glycine on Cu(100) and Comparison to Glycine on Cu(110). *J. Chem. Phys.* **2003**, *118*, 6059−6071.
(28) Hasselström, J.; Karis, O.; Weinelt, M.; Wassdahl, N.; Nilsson, A.; Nyberg, M.; Pettersson, L. G. M.; Samant, M. G.; Stöhr, J. The Adsorption Structure of Glycine Adsorbed on Cu (110); Comparison with Formate and Acetate/Cu(110). *Surf. Sci.* **1998**, *407*, 221−236.
(29) Rankin, R. B.; Sholl, D. S. Assessment of Heterochiral and Homochiral Glycine Adlayers on Cu(1 1 0) Using Density Functional Theory. *Surf. Sci.* **2004**, *548*, 301−308.
(30) Rankin, R. B.; Sholl, D. S. Structure of Enantiopure and Racemic Alanine Adlayers on Cu(1 1 0). *Surf. Sci.* **2005**, *574*, L1−L8.
(31) Rankin, R. B.; Sholl, D. S. Structures of Glycine, Enantiopure Alanine, and Racemic Alanine Adlayers on Cu(110) and Cu(100) Surfaces. *J. Phys. Chem. B* **2005**, *109*, 16764−16773.
(32) Mahapatra, M.; Burkholder, L.; Bai, Y.; Garvey, M.; Boscoboinik, J. A.; Hirschmugl, C.; Tysoe, W. T. Formation of Chiral Self-Assembled Structures of Amino Acids on Transition-Metal Surfaces: Alanine on Pd(111). *J. Phys. Chem. C* **2014**, *118*, 6856−6865.
(33) Baldanza, S.; Cornish, A.; Nicklin, R. E. J.; Zheleva, Z. V.; Held, G. Surface Chemistry of Alanine on Cu{111}: Adsorption Geometry and Temperature Dependence. *Surf. Sci.* **2014**, *629*, 114−122.
(34) Shavorskiy, A.; Eralp, T.; Schulte, K.; Bluhm, H.; Held, G. Surface Chemistry of Glycine on Pt{111} in Different Aqueous Environments. *Surf. Sci.* **2013**, *607*, 10−19.
(35) Eralp, T.; Ievins, A.; Shavorskiy, A.; Jenkins, S. J.; Held, G. The Importance of Attractive Three-Point Interaction in Enantioselective Surface Chemistry: Stereospecific Adsorption of Serine on the Intrinsically Chiral Cu{531} Surface. *J. Am. Chem. Soc.* **2012**, *134*, 9615−9621.
(36) Eralp, T.; Shavorskiy, A.; Held, G. The Adsorption Geometry and Chemical State of Lysine on Cu{110}. *Surf. Sci.* **2011**, *605*, 468−472.
(37) Eralp, T.; Shavorskiy, A.; Zheleva, Z. V.; Held, G.; Kalashnyk, N.; Ning, Y.; Linderoth, T. R. Global and Local Expression of Chirality in Serine on the Cu{110} Surface. *Langmuir* **2010**, *26*, 18841−18851.
(38) Thomsen, L.; Wharmby, M. T.; Riley, D. P.; Held, G.; Gladys, M. J. The Adsorption and Stability of Sulfur Containing Amino Acids on Cu{5 3 1}. *Surf. Sci.* **2009**, *603*, 1253−1261.
(39) Jones, G.; Jones, L. B.; Thibault-Starzyk, F.; Seddon, E. A.; Raval, R.; Jenkins, S. J.; Held, G. The Local Adsorption Geometry and Electronic Structure of Alanine on Cu{110}. *Surf. Sci.* **2006**, *600*, 1924−1935.
(40) Karagoz, B.; Reinicker, A.; Gellman, A. J. Kinetics and Mechanism of Aspartic Acid Adsorption and Its Explosive Decomposition on Cu(100). *Langmuir* **2019**, *35*, 2925−2933.
(41) Stöhr, J.; Jaeger, R. Absorption-Edge Resonances, Core-Hole Screening, and Orientation of Chemisorbed Molecules: CO, NO, and N_2 on Ni(100). *Phys. Rev. B: Condens. Matter Mater. Phys.* **1982**, *26*, 4111−4131.
(42) Stöhr, J. *NEXAFS Spectroscopy*; Springer: Berlin, 1996.
(43) Mohsenzadeh, A.; Bolton, K.; Richards, T. DFT Study of the Adsorption and Dissociation of Water on Ni(111), Ni(110) and Ni(100) Surfaces. *Surf. Sci.* **2014**, *627*, 1−10.
(44) Mohsenzadeh, A.; Richards, T.; Bolton, K. DFT Study of the Water Gas Shift Reaction on Ni(111), Ni(100) and Ni(110) Surfaces. *Surf. Sci.* **2016**, *644*, 53−63.
(45) Wang, S.-G.; Cao, D.-B.; Li, Y.-W.; Wang, J.; Jiao, H. Chemisorption of CO_2 on Nickel Surfaces. *J. Phys. Chem. B* **2005**, *109*, 18956−18963.
(46) O'Rourke, C.; Bowler, D. R. DSSC Anchoring Groups: A Surface Dependent Decision. *J. Phys.: Condens. Matter* **2014**, *26*, 195302.
(47) Tillotson, M. J.; Brett, P. M.; Bennett, R. A.; Grau-Crespo, R. Adsorption of Organic Molecules at the TiO_2(110) Surface: The Effect of van Der Waals Interactions. *Surf. Sci.* **2015**, *632*, 142−153.
(48) Kresse, G.; Furthmüller, J. Efficiency of Ab-Initio Total Energy Calculations for Metals and Semiconductors Using a Plane-Wave Basis Set. *Comput. Mater. Sci.* **1996**, *6*, 15−50.
(49) Kresse, G.; Furthmüller, J. Efficient Iterative Schemes for Ab Initio Total-Energy Calculations Using a Plane-Wave Basis Set. *Phys. Rev. B: Condens. Matter Mater. Phys.* **1996**, *54*, 11169−11186.
(50) Zhang, Y.; Yang, W. Comment on "Generalized Gradient Approximation Made Simple". *Phys. Rev. Lett.* **1998**, *80*, 890.
(51) Grimme, S.; Antony, J.; Ehrlich, S.; Krieg, H. A Consistent and Accurate Ab Initio Parametrization of Density Functional Dispersion Correction (DFT-D) for the 94 Elements H-Pu. *J. Chem. Phys.* **2010**, *132*, 154104.
(52) Grimme, S.; Ehrlich, S.; Goerigk, L. Effect of the Damping Function in Dispersion Corrected Density Functional Theory. *J. Comput. Chem.* **2011**, *32*, 1456−1465.
(53) Goerigk, L.; Grimme, S. A Thorough Benchmark of Density Functional Methods for General Main Group Thermochemistry, Kinetics, and Noncovalent Interactions. *Phys. Chem. Chem. Phys.* **2011**, *13*, 6670−6688.
(54) Goerigk, L.; Hansen, A.; Bauer, C.; Ehrlich, S.; Najibi, A.; Grimme, S. A Look at the Density Functional Theory Zoo with the Advanced GMTKN55 Database for General Main Group Thermochemistry, Kinetics and Noncovalent Interactions. *Phys. Chem. Chem. Phys.* **2017**, *19*, 32184−32215.
(55) Perdew, J. P.; Burke, K.; Ernzerhof, M. Generalized Gradient Approximation Made Simple. *Phys. Rev. Lett.* **1996**, *77*, 3865−3868.
(56) Blöchl, P. E. Projector Augmented-Wave Method. *Phys. Rev. B: Condens. Matter Mater. Phys.* **1994**, *50*, 17953−17979.
(57) Kresse, G.; Joubert, D. From Ultrasoft Pseudopotentials to the Projector Augmented-Wave Method. *Phys. Rev. B: Condens. Matter Mater. Phys.* **1999**, *59*, 1758−1775.
(58) Monkhorst, H. J.; Pack, J. D. Special Points for Brillouin-Zone Integrations. *Phys. Rev. B: Solid State* **1976**, *13*, 5188−5192.
(59) Makov, G.; Payne, M. C. Periodic Boundary Conditions in Ab Initio Calculations. *Phys. Rev. B: Condens. Matter Mater. Phys.* **1995**, *51*, 4014−4022.
(60) Birgersson, M.; Almbladh, C.-O.; Borg, M.; Andersen, J. Density-Functional Theory Applied to Rh(111) and CO/Rh(111) Systems: Geometries, Energies, and Chemical Shifts. *Phys. Rev. B: Condens. Matter Mater. Phys.* **2003**, *67*, 045402.
(61) Köhler, L.; Kresse, G. Density Functional Study of CO on Rh(111). *Phys. Rev. B: Condens. Matter Mater. Phys.* **2004**, *70*, 165405.
(62) Gotterbarm, K.; Luckas, N.; Höfert, O.; Lorenz, M. P. A.; Streber, R.; Papp, C.; Viñes, F.; Steinrück, H.-P.; Görling, A. Kinetics of the Sulfur Oxidation on Palladium: A Combined in Situ x-Ray

https://dx.doi.org/10.1021/acs.langmuir.0c01175
Langmuir XXXX, XXX, XXX−XXX

Photoelectron Spectroscopy and Density-Functional Study. *J. Chem. Phys.* **2012**, *136*, 094702.
(63) Ontaneda, J.; Bennett, R. A.; Grau-Crespo, R. Electronic Structure of Pd Multilayers on Re(0001): The Role of Charge Transfer. *J. Phys. Chem. C* **2015**, *119*, 23436−23444.
(64) Kahk, J. M.; Lischner, J. Core Electron Binding Energies of Adsorbates on Cu(111) from First-Principles Calculations. *Phys. Chem. Chem. Phys.* **2018**, *20*, 30403−30411.
(65) Pueyo Bellafont, N.; Viñes, F.; Hieringer, W.; Illas, F. Predicting Core Level Binding Energies Shifts: Suitability of the Projector Augmented Wave Approach as Implemented in VASP. *J. Comput. Chem.* **2017**, *38*, 518−522.
(66) Zdansky, E. O. F.; Nilsson, A.; MÅrtensson, N. CO-Induced Reversible Surface to Bulk Transformation of Carbidic Carbon on Ni(100). *Surf. Sci.* **1994**, *310*, L583−L588.
(67) Chen, M.; Lin, Z. Ab Initio Studies of Aspartic Acid Conformers in Gas Phase and in Solution. *J. Chem. Phys.* **2007**, *127*, 154314.
(68) Grau-Crespo, R.; Smith, K. C.; Fisher, T. S.; De Leeuw, N. H.; Waghmare, U. V. Thermodynamics of Hydrogen Vacancies in MgH_2 from First-Principles Calculations and Grand-Canonical Statistical Mechanics. *Phys. Rev. B: Condens. Matter Mater. Phys.* **2009**, *80*, 174117.
(69) Fukai, Y. *The Metal−Hydrogen System*; Springer: Berlin, 2005; Vol. *21*.

https://dx.doi.org/10.1021/acs.langmuir.0c01175
Langmuir XXXX, XXX, XXX−XXX